

# RSC Advances



This is an *Accepted Manuscript*, which has been through the Royal Society of Chemistry peer review process and has been accepted for publication.

*Accepted Manuscripts* are published online shortly after acceptance, before technical editing, formatting and proof reading. Using this free service, authors can make their results available to the community, in citable form, before we publish the edited article. This *Accepted Manuscript* will be replaced by the edited, formatted and paginated article as soon as this is available.

You can find more information about *Accepted Manuscripts* in the [Information for Authors](#).

Please note that technical editing may introduce minor changes to the text and/or graphics, which may alter content. The journal's standard [Terms & Conditions](#) and the [Ethical guidelines](#) still apply. In no event shall the Royal Society of Chemistry be held responsible for any errors or omissions in this *Accepted Manuscript* or any consequences arising from the use of any information it contains.

**Wettability and drag reduction of superhydrophobic aluminum surface**Haifeng Zhang<sup>a,b</sup>, Liang Yin<sup>a\*</sup>, Ling Li<sup>a</sup>, Shuyuan Shi<sup>a</sup>, Yang Wang<sup>a</sup>, Xiaowei Liu<sup>a,b</sup><sup>a</sup> MEMS Center, Harbin Institute of Technology, Harbin 150001, China<sup>b</sup> Key Laboratory of Micro-Systems and Micro-Structures Manufacturing, Ministry of Education, Harbin, 150001, China

\* Tel: +86 451 86413451; Fax: +86 451 86413441; e-mail: zhanghf@hit.edu.cn

**Abstract**

This present work reports a simple method to fabricate aluminum superhydrophobic surface using two-step procedure, the chemical etching and anodization. By varying the chemical etching and anodization time, we measured and compared the effects of morphological change on the wettability. The result indicates that the morphology is directly correlated to the wettability and adhesion ability. The resultant structure after the first step exhibits a high adhesion property. The high adhesion to low adhesion transition takes place after the anodization on the etched aluminum surface. The paper studies the effect of the adhesion on the liquid/solid friction drag. It is found that the adhesion has an obvious effect on friction drag. The drag reduction ratio for the low adhesion aluminum is about 50~60% compare with the high adhesion aluminum at low velocity. Such a property can be extensively used in the drag reduction field.

Keywords: Aluminum; Superhydrophobic surface; Adhesion; Drag reduction

**1. Introduction**

Friction is the force that resists the relative motion between two sliding surfaces, and it is frequently seen in daily life and in industrial manufacture.<sup>1,2</sup> Large amounts of energy are lost due to friction and it may also cause serious mechanical wear. Aluminum is widely used in various industrial fields as a basic material for numerous mechanical components. The control of

tribological interactions such as friction, adhesion and wear,<sup>3-5</sup> is necessary for both micro-scale devices and large-scale aluminum equipments, especially the accessibility of the moving parts.

Over the past decades, superhydrophobic aluminum surfaces have received significant attention in fluid reduction field due to their extraordinary surface properties.<sup>6,7</sup> Lots of nanostructured alumina surfaces including nanotips, nanowire arrays and nanowire pyramids have been prepared to improve the superhydrophobic property along with the wettability.<sup>8-12</sup> Up to date now, many researchers had prepared water-repellent surfaces, which show strong superhydrophobicity with low adhesion.<sup>13,14</sup> The superhydrophobic surfaces with high adhesion had also been fabricated using different methodology.<sup>15-18</sup> Recently, fluidic drag reduction efficiency of superhydrophobic surfaces has been investigated both theoretically and experimentally, and there are many successful examples.<sup>19-22</sup> However, previous studies mostly focused on numerical investigation and the fabrication of superhydrophobic surface. Few had discussed the influence of the adhesion ability upon drag reduction performance using experimental method. In this paper we proposed the fabrication of diverse nanostructured alumina surfaces using the combination of chemical etching and anodization, it was very economical and efficient. Meanwhile, the relationship was discussed between surface adhesion ability and drag reduction efficiency. It can hopefully play a guidance role on various engineering applications of the surface adhesion and anti-drag property.

## 2. Experimental

### 2.1. Sample preparation

Industrial grade aluminum foil (1 mm thickness, 99.5% purity, AA1050) was cut into 2×5 cm<sup>2</sup> pieces, then polished mechanically, and cleaned ultrasonically with acetone and ethanol in sequence to remove grease. The micro/nanoscale hierarchical structures of the alumina surface were simply produced through two-step chemical and electrochemical processes discussed as follows. The aluminum foil and a graphite plate were used as anode and cathode, respectively. The first step of the process involved simple chemical etching of an aluminum substrate in a

mixture solution of 0.1 M  $\text{CuCl}_2$  and 1 M HCl at 25 °C for 6 min, resulting in the formation of a microtextured surface composed of irregular, rectangle-shaped plateaus. After the reaction, the sample was rinsed thoroughly with deionized water. The second step, the etched aluminum foil was anodized in 0.3 M oxalic acid, under a constant current density of 500 mA  $\text{cm}^{-2}$  at the water bath for a suitable time. Then, to reduce the surface free energy, the cleaned aluminum foil was immersed in an ethanol solution containing 0.5% silane reagent (1H,1H,2H,2H-perfluorooctadecyltrichlorosilane) hexane for 100 min to tune the chemical compositions of the surface. The samples were heated at 120 °C for 1 h, thus the superhydrophobic alumina surfaces were obtained.

## 2.2 Characterization

The surface morphology was observed using a field-emission scanning electron microscope (FE-SEM, TESCAN VEGA). The contact angles (CA) and sliding angles (SA) were measured with 5  $\mu\text{L}$  droplets of water using an optical contact-angle meter system (Data Physics Instrument GmbH, Germany). The average CA and SA values were obtained by measuring each sample at a minimum of five different positions at room temperature. The drag reduction efficiency was measured by a self-designed water spraying system.

## 3. Results and discussion

### 3.1 Formation of micro/nanoscale hierarchical structures

To understand the formation of the micro-nanostructure on a superhydrophobic aluminum surface, a morphology comparison of the smooth aluminum surface, chemical etching aluminum surface is shown in Fig.1. Fig. 1 shows SEM images of the surface morphology of (a) untreated aluminum surfaces and (b) chemical etching aluminum surfaces in 0.1 M  $\text{CuCl}_2$  and 1 M HCl solution for 6 min. It can be seen that the untreated aluminum foil used here has a smooth surface without any micro-or nanostructure (Fig. 1(a)). When the aluminum foil is chemical etching in 0.1 M  $\text{CuCl}_2$  and 1 M HCl aqueous solution for 6 min, the entire aluminum surface is rough and composed of irregular “protrusions”. The high-resolution SEM image shown in Fig. 1(b) confirms

that the etched aluminum surface consists of irregular rectangular plateaus. The plateaus are 2-5  $\mu\text{m}$  in size and are distributed throughout the surface consistently.

In order to introduce nanoscale structure on the entire etched surface, the etched specimens were anodized.<sup>23-27</sup> The traditional anodization of aluminum surface was usually performed in acid electrolytes, including sulphuric acid, oxalic acid and phosphoric acid under a low voltage.<sup>28-30</sup> In this study, the anodization was conducted with a high constant current density of  $500 \text{ mA cm}^{-2}$  (120 V) in 0.3 M oxalic acid, at the water bath with a magnetic stirrer stirring. The anodization of the aluminum foil leads to a porous morphology. The formation mechanism of the nanoporous alumina is involved with the electric field-assisted processes of barrier formation and nanopores dissolution.<sup>31-34</sup> Fig. 2 shows the top-view SEM images of the alumina film fabricated in oxalic acid under the high-field anodization, exhibiting a dynamic evolution process of the surface morphologies from nanopores, nanowire, and then to collapsed nanowire. Fig. 2(a) shows the nanoporous structure formed with an anodization time of 4 min. Nanopores formed on the surface are distributed randomly. As the increase of anodization time, the rate of which is also accelerated, verifying the increment of pore density and the enlargement of pore size. At the same time, the walls between two adjacent pores become thinner and thinner until being broken up at about 7 min and there follows a subsequent nanowire occurrence. It can be seen from the inserted image of Fig. 2(b), the entire surfaces of which are covered with nanopores and nanowires. This honeycomb-like surface (Fig.2(b)) with a nanopore diameter ranging from 100 to 200 nm provided a good micro/nanoscale hierarchical structures. In addition, the stress is generated at the bottom of the nanopores due to the volume expansion along with the conversion of metal into oxides. The morphology evolution characteristic of nanostructures can be attributed to the concentration gradient of the oxalic-acid solution along the nanoporous channels. For a rapid supply rate, the concentration of oxalic-acid solution around the porous alumina surface could be higher than that at the bottom of the nanopores, leading to the quicker dissolution of the porous alumina at the surface than at the bottom. When the nanopore is widely expanded, the

oxalic-acid concentration along nanopore channels become nearly homogeneous and the released heat is easily dissipated, which will slow down the oxalic-acid etching process. When alumina nanowires further become smaller and longer, they will collapse eventually due to the gravity and stirring effects as shown in Fig. 2(c). The stress analysis at the bottom of nanopores is illustrated in Fig. 2(d). The stress  $F$  at point  $p$  can be resolved into  $F1$  and  $F2$ . The longitudinal component force ( $F2$ ) pushes the oxides layer upward, while the resultant force of the lateral component force ( $F1$ ) increases the inner stress and contributes to the formation of regular block from the surface crack. The surface crack of alumina films cannot happen if a low-temperature electrolyte system and low field anodization are supplied, which can be aptly explained by the fact that the expansion velocity and the inner stress of the alumina are very small in this condition.

### 3.2 Wettability and adhesion properties

The wettability of the as-prepared aluminum surfaces is characterized by water static CA measurements. First-step and second-step resultant surfaces after modification exhibit different wettabilities and adhesion properties, even though both of them are superhydrophobic with contact angles over  $150^\circ$ . Fig. 3 shows the images of water droplets on the first-step fabricating superhydrophobic aluminum surfaces (sample A, chemically etching about 6 min) and the second-step anodized fabricating superhydrophobic aluminum surfaces (sample B, electrochemical anodization about 7 min after chemically etching ) both after modification. The water CA for two sample surfaces are  $153^\circ \pm 2^\circ$  and  $160^\circ \pm 2^\circ$ , respectively. From Fig.1 we can see that the first-step surfaces have only sub-microstructure, the bottom of water droplet tends to penetrate into the rough grooves, resulting in a larger rolling angle. As shown in Fig.3(a), the water droplet stays still even when sample A is tilted vertically ( $90^\circ$ ) or even turned upside down ( $180^\circ$ ), demonstrating a strong water adhesion ability. This case is well explained by the Wenzel model, in which, the water droplets pin the surface tightly, thus form a high contact angle hysteresis.<sup>35</sup> After the second-step anodization, the characteristics of the modified sample

surface successfully change from Wenzel state to Cassie–Baxter state. The CAs of the intermediate films obtained at various time of 0, 4, 7 and 10 min are  $153^{\circ} \pm 2^{\circ}$ ,  $155^{\circ} \pm 2^{\circ}$ ,  $160^{\circ} \pm 2^{\circ}$  and  $156^{\circ} \pm 2^{\circ}$ , respectively. The contact angles increase with the increment of anodization time until 7 min and then decrease with the further increment of anodization time. The maximum contact angle  $160^{\circ} \pm 2^{\circ}$ , is achieved on the modified surface at the anodization time of 7 min (Fig. 3(b)). The Water SA of the modified films changed obviously with the reaction time, with values of  $180^{\circ}$ ,  $20^{\circ}$ ,  $2^{\circ}$ , and  $5^{\circ}$ , respectively, for 0, 4, 7, and 10 min. Therefore, the wettability and adhesion of the samples can be regulated by altering anodization time. A 5  $\mu$ L water droplet cannot steadily sit on the surface of sample B tilted by  $\sim 2^{\circ}$ . The surface of sample B has a micro/nanoscale hierarchical structures and trap lots of air pockets, just as described by Cassie–Baxter model.<sup>36,37</sup> The air pockets increases the triple contact line and decreases the proportion of wetted surface.

Moreover, the modified sample B shows not only superhydrophobicity but also superoleophobicity. The liquid droplets with various surface energy exhibit typical spherical shapes on the sample surface, as shown in Fig. 4. The contact angles of water ( $72 \text{ mN m}^{-1}$ ,  $20^{\circ}\text{C}$ ), crude oil ( $35 \text{ mN m}^{-1}$ ,  $20^{\circ}\text{C}$ ) and peanut oil ( $28.2 \text{ mN m}^{-1}$ ,  $20^{\circ}\text{C}$ ) are  $160^{\circ} \pm 2^{\circ}$ ,  $151^{\circ} \pm 2^{\circ}$  and  $151^{\circ} \pm 2^{\circ}$ , respectively. Peanut oil droplets did not stick on the etched surface and rolled off from the surface when tilted to  $15^{\circ}$ . The size of the nanopores or the porosity of the etched pore walls is an important factor for oil repellency. The nanopores produce the effective re-entrant structure, and hence oil effectively pin at the nanopores developed on the pit walls close to the top surface. The suppression of the oil penetration by nanopores effectively enhances the roll-off rate of the oil droplet on the tilted surface.

### 3.3 Analysis of the mechanical stability

The lack of the stability is a common problem for most of the fabricated superhydrophobic surfaces, which restricts their prospects in industrial applications. We used the same method with

Barthwal to estimate the mechanical stability.<sup>38</sup> In our study, the scotch tape test was applied to examine the stability and adhesion of the fabricated superhydrophobic aluminum surface. Fig.5 reveals the FE-SEM images of the aluminum surface before and after the tape test. We repeated the peeling test up to 6 times. Fig. 5a-c shows the FE-SEM images of the aluminum surface before and after different peeling attempts. Compared with the original film surface, the images clearly indicated no damage or detachment of the film after the peeling tests. Fig. 5(d) shows the CA and SA measured after each peeling attempt, we can see that the CA and SA have only slight change. It is also confirmed that the fabricated film has a good mechanical stability and retains its superhydrophobic after the tape test. This can be explained insitu growth thick alumina films on the aluminum substrates. The anodized aluminum surfaces possess an improved chemical resistance and a higher micro hardness compared with the untreated aluminum.<sup>39-42</sup>

### 3.4 Stability of air-water interface

The hydrostatic pressure plays an important role in the wetting transitions. When hydrostatic pressure is comparable to or even higher than the capillary pressure, the wetting transition from the Cassie–Baxter state to the Wenzel state will occurred on superhydrophobic surfaces.<sup>43,44</sup> It maybe increase the liquid/solid friction drag. Therefore, the stable composite interface is essential for drag reduction of superhydrophobic surfaces. In this subsection, we study the condition under which the air water interface (meniscus) may transition from the nonwetted state (Cassie state) to the wetted state (Wenzel state). This is important in practical applications for drag reduction because once the thin gas layer is replaced by the liquid, none of the beneficial effects remain. If entrapped gas is to exist under a superhydrophobic surface, two conditions must be met. First, the liquid-gas interface under the drop must be able to be in a state of force equilibrium. Second, the asperities must be tall enough that liquid protruding between them does not contact the underlying solid.<sup>45,46</sup> For a given surface texture geometry, there exists a critical hydrostatic pressure (i.e., maximum immersion depth) at which the air-water interface may no more stay pinned at the surface asperities.

In this work we proposed a simple wetting mode of the air/water/ pillar (A/W/P) interface as shown in Fig.6. The air diffusion into and out of the liquid is neglected. According to the Young-Laplace equation for the pressure difference between two sides of the interface can be written as Eq. 1.<sup>47,48</sup>

$$P_L - P_G = \frac{2\gamma}{R} \quad (1)$$

where  $P_L$  and  $P_G$  are the pressure of the liquid near the top interface of the drop and the atmosphere pressure, respectively.  $\frac{2\gamma}{R}$  is the pressure induced by the surface tension ( $72.8 \times 10^{-3}$  Nm in the case of water),  $R$  is curvature radius of the liquid-gas interface (shown in Fig.6 (a)). As Eq. (1), only when the curvature radius of the liquid-gas interface is small enough, thermodynamic equilibrium can be maintained.

Fig. 6(a) schematically shows the microscopic contact state of the superhydrophobic surface underwater when the hydraulic pressure is less than the atmosphere pressure  $P_G$ . Water is suspended on the top of the pillar, and the spaces within the pillar formed an air layer, indicating an air/water/ pillar (A/W/P) interface underwater. On the other hand, after the hydraulic pressure exceeded the critical value  $P_G$ , the water penetrates into the spaces within the pillar, and the A/W/P interface does not exist. Moreover, the existence of a multi-scale pillar increases the contact area between the water and solide surface, enhances the total adhesion between the water and solid surface according to the smooth solid/liquid interface theory.

If sufficiently small, drops retain spherical proportions, the drop radius,  $R$ , can be written as eq.2.<sup>49</sup>

$$R = \frac{D}{2 \cos(\pi - \theta_a + \alpha)} \quad (2)$$

where  $D$  is the cavity length of the superhydrophobic geometry,  $\theta_a$  is the contact angle. Combining Eq. (1) and Eq. (2), Eq. (3) can be deduced.

$$P_L - P_G = \frac{4\gamma \cos(\pi - \theta_a + \alpha)}{D} \quad (3)$$

From the Fig.1 (b) and Fig.2 (b) we can see that the etched aluminum surface has only submicrostructure, however the anodized aluminum surface has micro/nanoscale hierarchical structures. According to the Eq. (3), the anodized aluminum surface can be easily maintained the Cassie state, due to the cavity length  $D$  of the anodized aluminum surface smaller than the etched aluminum surface.

### 3.5 The drag reduction property of the as-prepared surfaces

In order to estimate the drag reduction property of different adhesion properties, an experimental setup of the liquid/solid friction drag was reported.<sup>50</sup> Fig. 7(a) shows the schematic for testing the drag reduction efficiency of the as-prepared surfaces. A force sensor was introduced between the two sliding pairs to measure the friction drag between the flat flow and the fixed superhydrophobic surface. The tested samples were cut into a size of  $1.5 \times 1.0 \text{ cm}^2$  and fixed at the bottom of the force sensor. The copper nozzle with a caliber of  $1.5 \times 1.0 \text{ cm}^2$  was used to release the flat flow, which was provided by a water pump. The flowmeter was introduced to adjust the flow rate. The friction drag of the solid-liquid interface was transformed into an electric signal and collected by an external data acquisition system and then computed by a computer.

The drag reduction properties of the different adhesion surface were measured for 5 s with the same flow rate. The average values were ultimately selected as the friction drag of the corresponding surface. Moreover, the friction drag was also measured under different flow rates to investigate the influence of the flow rate on the drag reduction performance. As shown in Fig.7 (b), we can see that the sample B has the lowest friction drag, while the sample A has an obvious effect of drag increase comparing with the sample B. The drag reduction ratio for the sample B is about 50~60% compare with the sample A. This phenomenon can be aptly explained by that the magnitude of hydrodynamic slippage which characterizes the anti-drag performance

is closely linked to the wettability of a special structured surface. Qualitatively, for the second-step fabricating surface, there is a large but not continuous liquid-air contact layer which prevents the interaction of liquid and solid surface. Thus it is extremely hard for liquid momentum parallel to the interface to transfer, and as a consequence, a long slip length is generated. While for the first-step fabricating surface which exhibits pretty high adhesion ability, most of the momentum wastes at the interface,<sup>14</sup> resulting in a slippage which is too short to be taken into account. From the Fig. 7(b), we can see that the flow velocity can affect the effect of the drag reduction. The drag reduction ratio for the sample B is 30~40% at low velocity. When the flow velocity was about  $4.5 \text{ m s}^{-1}$ , the drag reduction ratio of the sample B reduced to 20~30%. The reason is that higher flow velocities cause faster removal rates of the surface air layer in flowing water. The disappearance of entrapped gas would cause declining drag reduction because of decreasing slippage. With increasing flow velocity, a rise in drag was observed, which was attributed to the morphology of the surface air layer and its depletion by high shear flow.

To testify the rationality of the drag reduction experiment, a 2D finite-element method (Comsol Multiphysics v4.2) was used to build three models to simulate the roughness of different surfaces. The models solved the Navier-Stokes equations for a steady pressure-driven flow through the channels with different slip conditions. We analyzed both the high adhesion case and the low adhesion case. Fig. 8 shows the numerical results of the pressure-driven flow over different surfaces. For reaching a conclusion through data, a graph exhibiting the relationship between the shear rate and the inflow velocity was also given, as shown in Fig. 8(d). From Fig. 8(d), it can be easily recognized that the surface with a lower adhesion property has a lower shear rate, which suggests that the superhydrophobic surfaces with low adhesion ability can be used in drag reduction field. However, for the surface with high adhesion ability, the shear rate is much higher, and it will increase friction instead. In general, the modeling results are aptly in accordance with the experimental results.

#### 4. Conclusion

In conclusion, we have demonstrated a simple and inexpensive method to prepare superhydrophobic surfaces on aluminum foil by a combination of chemical etching and anodization. The adhesion properties of the aluminum surface can be controlled by the surface morphologies. The water contact angles are  $153^{\circ} \pm 2^{\circ}$  and  $160^{\circ} \pm 2^{\circ}$  for the chemical etching and anodization aluminum foil, respectively. However, the chemical etching sample has a good superhydrophobicity with high adhesion ability, the second step anodization has successfully changed the adhesion ability of the as-prepared surface from high to low. The drag testing verifies that our obtained alumina surface with low adhesion ability possesses a drag reduction ratio of 30~40% at low velocity. Such a superhydrophobic surface can be extensively used in the drag reduction field.

#### Acknowledgements

This work was supported by National Basic Research Program of China (No.2012CB934104), National Science Foundation of China (No. 61474034), Natural Science Foundation of Heilongjiang Province of China (NO: F201418), the Fundamental Research Funds for the Central Universities (Grant No. HIT.NSRIF.2014040, HIT.NSRIF.2013040).

#### Notes and references

- 1 M.R. Cai , R. S. Guo , F. Zhou , and W. M. Liu , Sci. China Ser. E., 2013, 56(12), 2888-2913 .
- 2 B. Dean, and B. Bhushan, Phil. Trans. R. Soc. A, 2010, 368, 4775-4806.
- 3 J. Y. Leong, T. Reddyhoff, S. K. Sinha, A. S. Holmes, and H. A. Spikes, Tribol Lett, 2013, 49:217-225.
- 4 H.A. Spikes, Proc. Inst. Mech. Eng. J, 2003, 217, 1-14.
- 5 H.A. Spikes, Proc. Inst. Mech. Eng. J, 2003, 217, 15-26.
- 6 Y. Wu, Q.B Wei, M.R Cai, and F. Zhou, Adv. Mater. Interfaces 2015, 2, 1400392,1-15.

- 7 Y.L. Zhang, H Xia, E Kim, and H.B Song, *Soft Matter*, 2012, 8, 11217-11231.
- 8 S. Peng, D. Tian, X. J.Yang, and W.L. Deng, *ACS Appl. Mater. Interfaces*, 2014, 6(7), 4831-4841.
- 9 B. G. Park, W. Lee, J. S. Kim, and K. B. Lee. *Colloids Surf., A*. 2010, 370, 15-19.
- 10 L. J. Liu, F. Y. Xu, Z. L. Yu, and P. Dong. *Appl. Surf Sci.* 2012,258,8928-8933.
- 11 S. Gogte, P. Vorobieff, R. Trusdell, and A. Mammoli, *Phys. Fluids*, 2005, 11, 051701.
- 12 J. Cui, W.Z. Li, and W. Lam, *Comput. Math. Appl.*, 2011, 61, 3678-3689.
- 13 A.A Hayder, D.M Hassan, and B.Y. Zulkefli, *ChemBioEng Rev*, 2015, 2,1-20.
- 14 Y Liu, J Liu, S Li, Z Han, S Yu, and L Ren, *J. Mater. Sci.*, 2014, 49(4), 1624-1629.
- 15 Y Liu, J Liu, S Li, Y Wang, Z Han, and L Ren, *Colloids Surf., A.*, 2015, 466, 125-131.
- 16 Y Liu, S Li, J Zhang, Y Wang, Z Han, and L Ren, *Chem. Eng.J.*, 2014, 248(15), 440-447.
- 17 Y Liu, J Liu, S Li, J Liu, Z Han, and L Ren, *ACS Appl. Mater. Interfaces*, 2013, 5(18), 8907-8914
- 18 Q Liu, X Tong, and G Zhou, *Langmuir*, 2015, 31(48), 13117-13126.
- 19 F.H. Cao, Z. Zhang, Y.L. Cheng, J.F. Li, J.Q. Zhang, J.M. Wang, and C.N. Cao, *Acta Metall.Sin*, 2003, 16, 22-30.
- 20 M. A. Samaha, H. V. Tafreshi, and M. Gad-el-Hak, *Colloids Surf., A.*, 2012, 399, 62-70
- 21 M.J. Cheng, M.M Song, H.Y. Dong, and F shi, *Small*, 2015,11,1665-1671.
- 22 L. Balázs, and J.-F. Gouyet, *Physica A*, 1995, 217, 319-338.
- 23 L. Y. Yao, M. J. Zheng, L. Ma, W. Li, M Li, W. Li, M. Li, and W.Z. Shen, *Mater. Res. Bull*, 2011, 46(9), 1403-1408.
- 24 G E Thompson, *Thin Solid Films*, 1997, 297, 192-201.
- 25 S.J. Garcia-Vergara, P. Skeldon, G.E. Thompson, H. Habazaki, *Electrochim. Acta*, 2006, 52, 681-687
- 26 J. E. Houser, and K. R. Hebert, *Nature mater.*, 2009, 8, 415-419.
- 27 K. Nakayama, E. Tsuji, Y. Aoki, and H. Habazaki, *RSC Adv.*, 2014, 4, 30927-30933.

- 28 X.L. Wang, X. J. Liu, F. Zhou, and W. M. Liu, *Chem. Commun.*, 2011, 47, 2324-2326.
- 29 W J. Stepniowski, M. Norek, M. Michalska-Domańska, and Z. Bojar, *Mater. Lett.*, 2013, 111, 20-23.
- 30 K. Ersching, E. Dorico, R.C. da Silva, V.C. Zoldan, E.A. Isoppo, A.D.C. Viegasa, and A.A. Pasa, *Mater. Chem. Phys.*, 2012, 137, 140-146.
- 31 D Lo, and R. A Budiman, *J. Electrochem. Soc.*, 2007, 154, C60-C66.
- 32 K. Kim, J. Choi, and J T Lee, *Trans. Electr. Electron. Mater.* 2010, 11(5), 230-233.
- 33 A. M. Abd-Elnaiem, and A. Gaber, *Int. J. Electrochem. Sci.*, 2013, 8, 9741-9751.
- 34 T. Y. Kima, and S. H. Jeong, *J. Chem. Eng.*, 2008, 25, 609-611.
- 35 T. Darmanin, E. Taffin de Givenchy, S. Amigoni, and F. Guittard, *Adv. Mater.*, 2013, 25, 1378-1394.
- 36 Y.C. Jung, and B. Bhushan, *J. Phys. Condens. Matter.* 2010, 22, 035104.
- 37 R.J. Daniello, N.E. Waterhouse, and J.P. Rothstein, *Phys. Fluids* 21 (2009) 085103.
- 38 S. Barthwal, Y.S. Kim, and S.H. Lim, *Langmuir* 2013, 29, 11966-11974.
- 39 C. W. Extrand, *Langmuir* 2002, 18, 7991-7999.
- 40 C. W. Extrand, *Langmuir* 2004, 20, 5013-5018.
- 41 T. H. Fang, T.H. Wang, S.H. Kang, and C.H. Chuang, *Curr. Appl. Phys.*, 2009, 9(4), 880-883.
- 42 S Caporali, A Fossati, and U Bardi, *Corros. Sci.*, 2010, 52, 235-241.
- 43 N A. Patankar, *Langmuir* 2010, 26(11), 8941-8945
- 44 D Murakami, H Jinnai, and A Takahara, *Langmuir* 2014, 30, 2061-2067.
- 45 C. W. Extrand, *Langmuir* 2004, 20, 5013-5018.
- 46 J. D. Wang, and D.R. Chen, *Langmuir* 2008, 24, 10174-10180.
- 47 M.M. Amrei, and H. V. Tafreshi, *Colloids Surf., A*, 2015, 481, 547-560.
48. J. D. Wang, H. S. Chen, T Sui, A Li, and D.R. Chen, *Plant Sci.* 2009, 176(5), 687-695.
- 49 B Wang, J.D. Wang, and D.R. Chen, *Acta Phys. Sin.* 2014, 63(7), 074702.
- 50 Y Wang, X.W. Liu, H.F. Zhang, and Z.P. Zhou, *RSC Adv.*, 2015, 5, 18909-18914.

## Figure captions

**Fig. 1** SEM images of the surface morphology of (a) untreated aluminum surfaces and (b) chemical etching aluminum surfaces in 0.1 M  $\text{CuCl}_2$  and 1 M HCl solution for 6 min.

**Fig. 2** SEM images of the aluminum surfaces etched in solutions containing 0.1 M  $\text{CuCl}_2$  and 1 M HCl, and then anodized in 0.3 M oxalic acid electrolyte at a constant current of 500mA under an water bath environment for (a) 4 min (b) 7 min (c) 10 min (d) Schematic depiction of the evolution of surface morphology

**Fig. 3** CAs of water droplets on: (a) chemical etched aluminum surfaces about 6 min in 0.1M  $\text{CuCl}_2$  and 1 M HCl solution and (b) anodized alumina surfaces about 7 min in 0.3 M oxalic acid solution.

**Fig. 4** Wettability photo of the different liquid droplets water droplets on the anodized superhydrophobic aluminum surface

**Fig. 5** SEM images of fabricated aluminum surfaces: (a) bare aluminum surface; (b) after three times peeling test; (c) after six times peeling tests.

**Fig. 6** (a and b) Model illustration to explain the states of air layer on solid surface underwater when the hydraulic pressure  $P_L$  is below and above the critical value of  $P_G$ , respectively.

**Fig.7** (a) Schematic of the frictional measurement. (b) Friction drags versus the velocity of the water flowing over surfaces with different adhesion property.

**Fig.8** Numerical results of the pressure-driven flow over different surfaces: (a) high adhesion surface; (b) low adhesion surface; (c) flat surface without any treatment. The color bar refers to the velocity, which is given in meters per second. The inflow velocity for all cases is  $2 \text{ m s}^{-1}$ . (d) The shear rate versus the inflow velocity of the pressure-driven flow over surfaces with different adhesion property

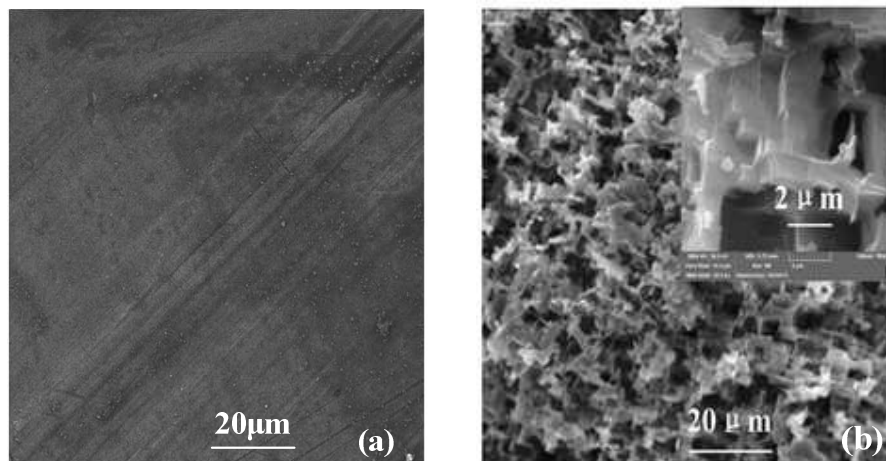


Fig. 1 SEM images of the surface morphology of (a) untreated aluminum surfaces and (b) chemical etching aluminum surfaces in 0.1 M  $\text{CuCl}_2$  and 1 M HCl solution for 6 min.

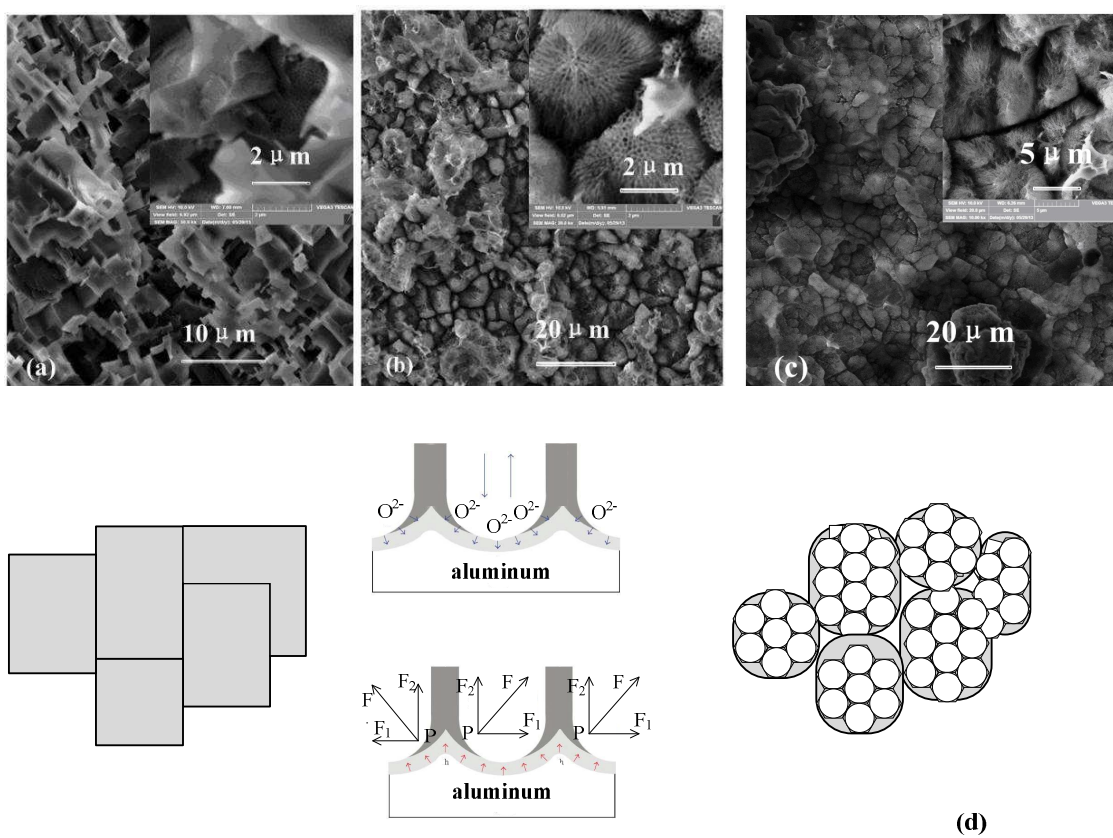


Fig. 2 SEM images of the aluminum surfaces etched in solutions containing 0.1 M  $CuCl_2$  and 1 M HCl, then anodized in 0.3 M oxalic acid electrolyte at a constant current of 500mA under a water bath environment for (a) 4 min (b) 7 min (c) 10 min (d) Schematic depiction of the evolution of surface morphology

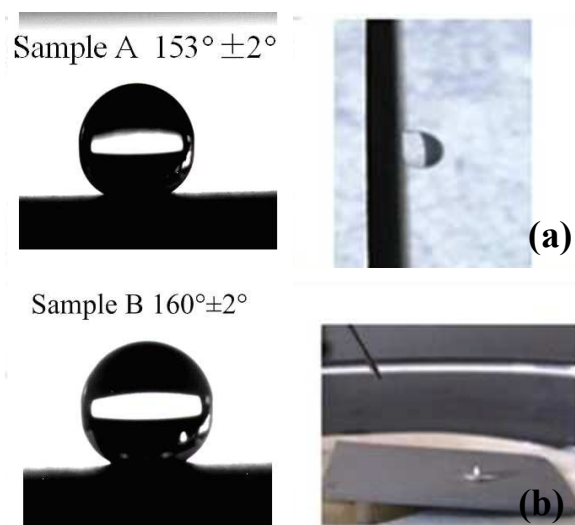


Fig. 3 CAs of water droplets on: (a) chemical etched aluminum surfaces about 6 min in 0.1M  $\text{CuCl}_2$  and 1 M HCl solution and (b) anodized alumina surfaces about 7 min in 0.3 M oxalic acid solution.

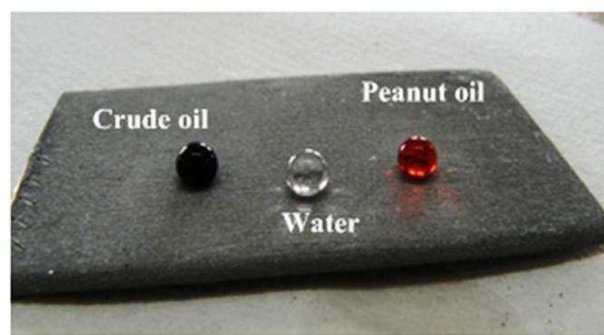


Fig. 4 Wettability photo of the different liquid droplets water droplets on the anodized superhydrophobic aluminum surface

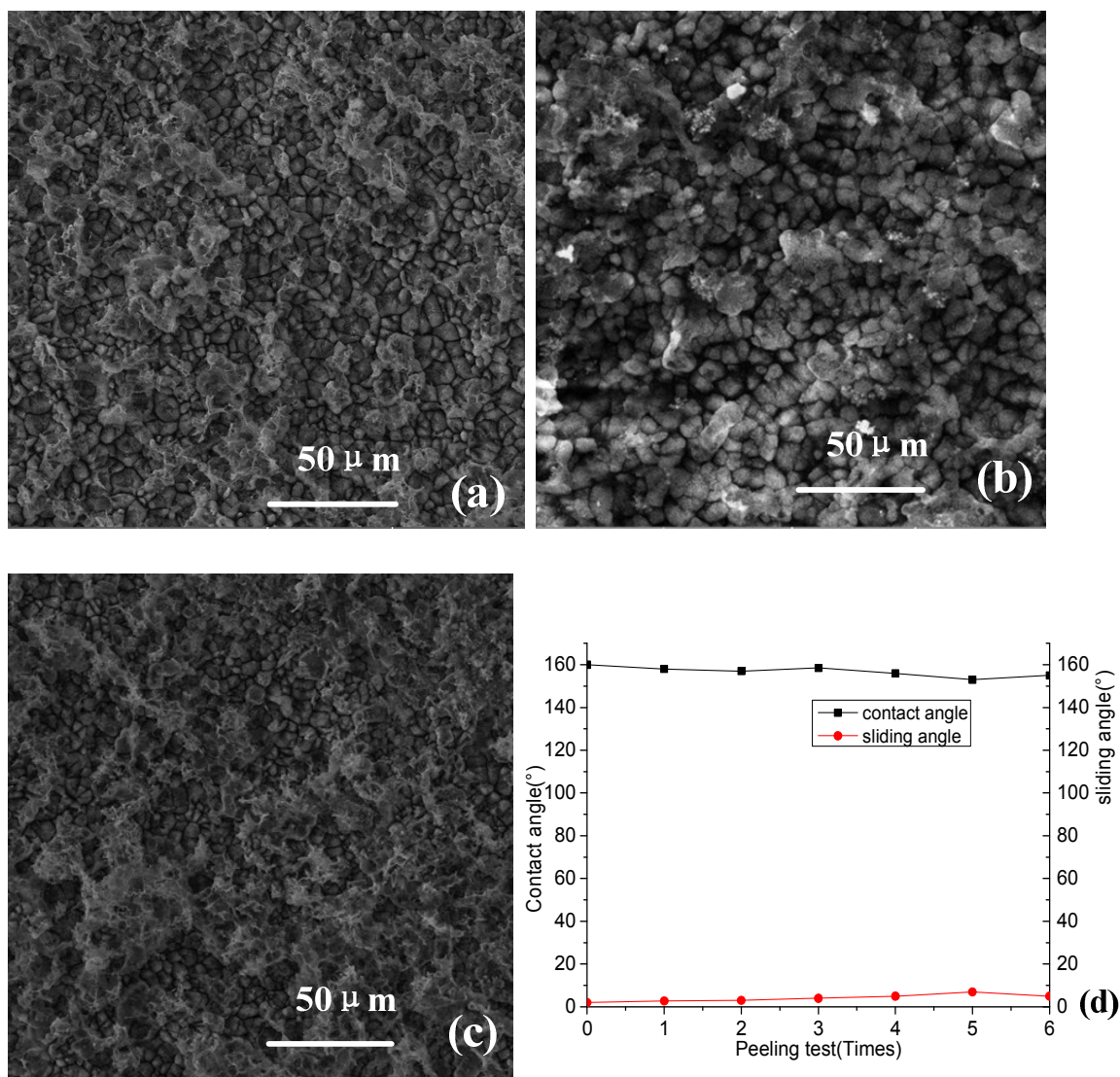


Fig. 5 FE-SEM images of fabricated aluminum surfaces: (a) bare aluminum surface; (b) after three times peeling test; (c) after six times peeling tests. (d) curve showing CA and SA measured with respect to peeling test on a fabricated aluminum surfaces

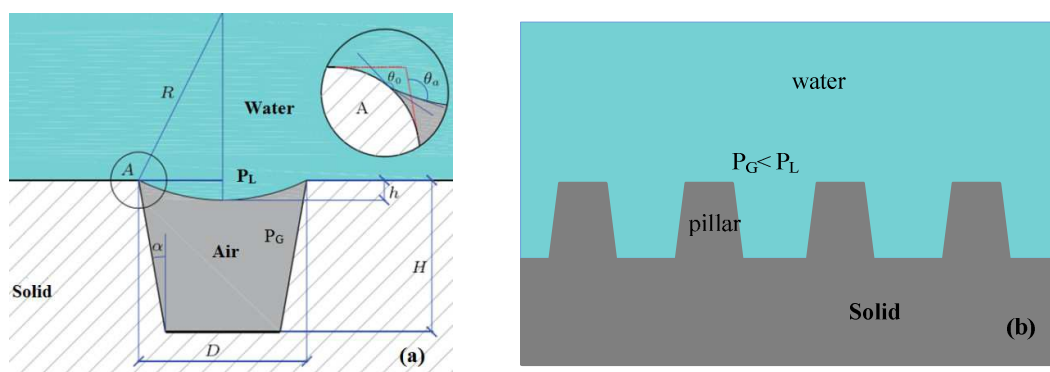


Fig. 6 (a and b) Model illustration to explain the states of air layer on solid surface underwater when the hydraulic pressure  $P_L$  is below and above the critical value of  $P_G$ , respectively.

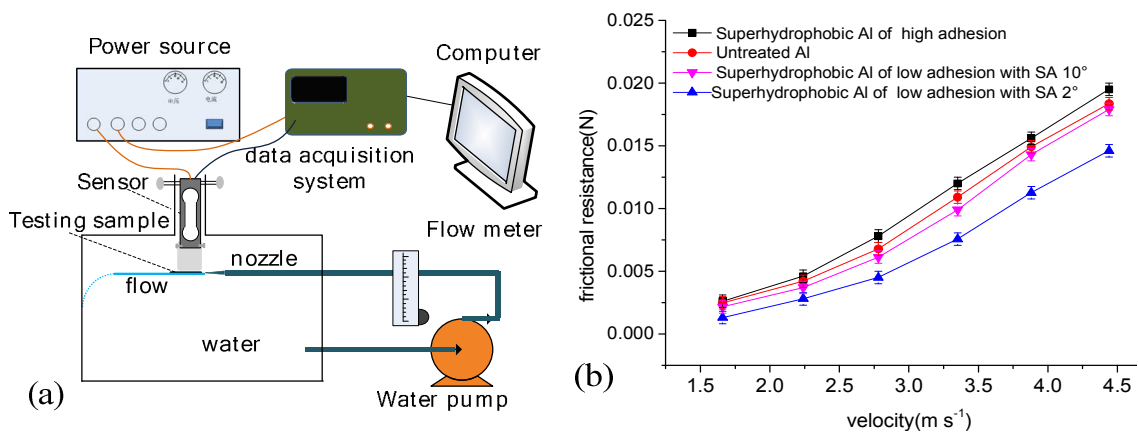


Fig.7 (a) Schematic of the frictional measurement. (b) Friction drags versus the velocity of the water flowing over surfaces with different adhesion property.

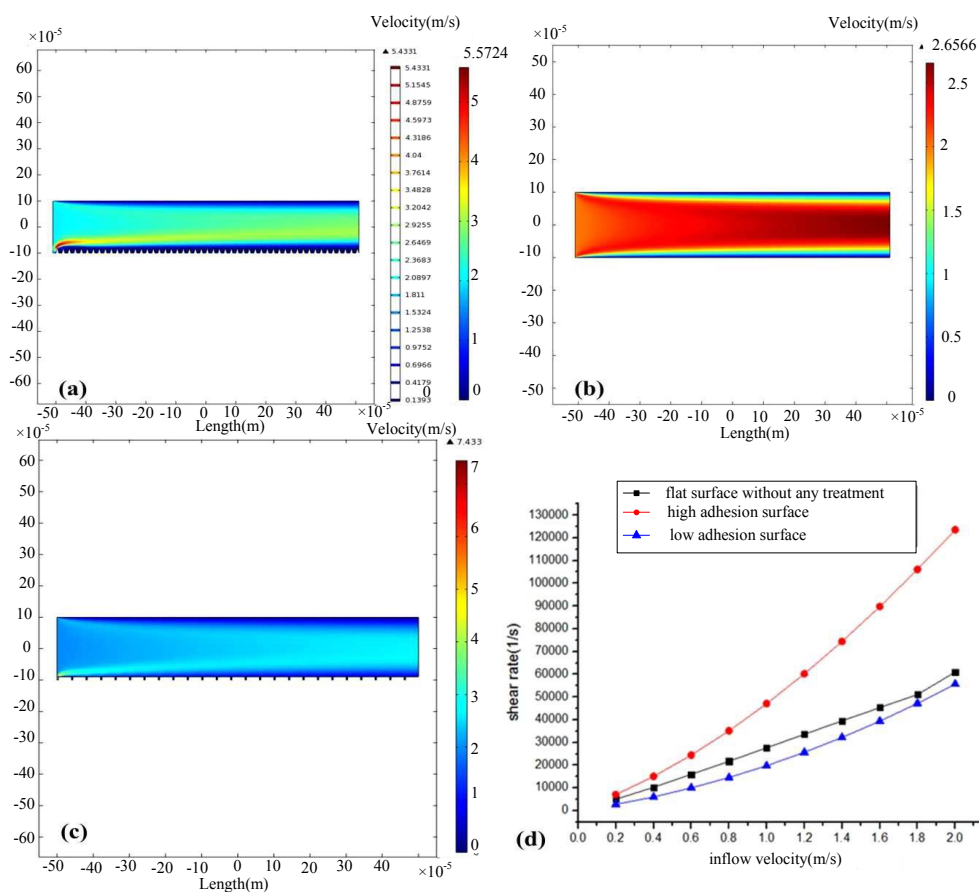
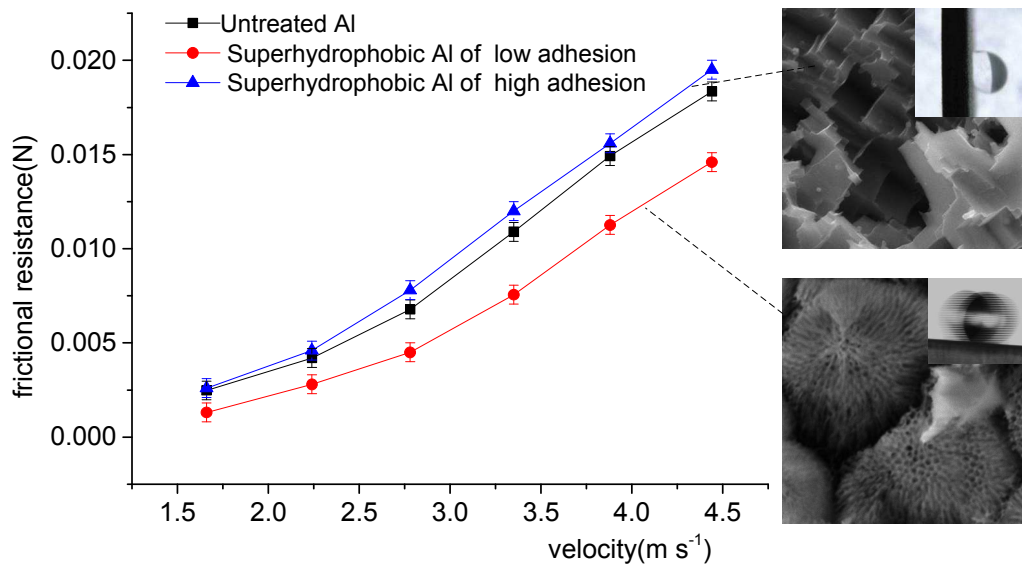


Fig 8. Numerical results of the pressure-driven flow over different surfaces: (a) high adhesion surface, (b) low adhesion surface, (c) flat surface without any treatment. The color bar refers to the velocity, which is given in meters per second. The inflow velocity for all cases is  $2 \text{ m s}^{-1}$ , (d) The shear rate versus the inflow velocity of the pressure-driven flow over surfaces with different adhesion property

## Graphical abstract



The friction drag versus the velocity of the water flowing over surfaces with different adhesion property